On the two-dimensionalization of quasi-static MHD turbulence

Benjamin Favier, Fabien Godeferd, Claude Cambon, Alexandre Delache

▶ **To cite this version:**

Benjamin Favier, Fabien Godeferd, Claude Cambon, Alexandre Delache. On the two-dimensionalization of quasi-static MHD turbulence. Physics of Fluids, 2010, 22 (7), pp.075104. 10.1063/1.3456725 . hal-00516503

HAL Id: hal-00516503
https://hal.science/hal-00516503

Submitted on 9 Sep 2010

HAL is a multi-disciplinary open access archive for the deposit and dissemination of scientific research documents, whether they are published or not. The documents may come from teaching and research institutions in France or abroad, or from public or private research centers.

L'archive ouverte pluridisciplinaire **HAL**, est destinée au dépôt et à la diffusion de documents scientifiques de niveau recherche, publiés ou non, émanant des établissements d'enseignement et de recherche français ou étrangers, des laboratoires publics ou privés.

On the two-dimensionalization of quasi-static MHD turbulence

B. Favier,[1, a)] F.S. Godeferd,[1] C. Cambon,[1] and A. Delache[2]

[1)] *LMFA UMR 5509 CNRS, École Centrale de Lyon, Université de Lyon, France*

[2)] *LaMUSE EA 3989, Université Jean Monnet, Saint-Étienne, France*

(Dated: 28 May 2010)

We analyze the anisotropy of turbulence in an electrically conducting fluid in the presence of a uniform magnetic field, for low magnetic Reynolds number, using the quasi-static approximation. In the linear limit, the kinetic energy of velocity components normal to the magnetic field decays faster than the kinetic energy of component along the magnetic field [Moffatt, JFM 28, 1967]. However, numerous numerical studies predict a different behavior, wherein the final state is characterized by dominant horizontal energy. We investigate the corresponding nonlinear phenomenon using Direct Numerical Simulations. The initial temporal evolution of the decaying flow indicates that the turbulence is very similar to the so-called "two-and-a-half-dimensional" flow [Montgomery & Turner, Phys. Fluids 25(2), 1982] and we offer an explanation for the dominance of horizontal kinetic energy.

PACS numbers: 47.27.E-, 47.27.Gs, 47.65.-d

Keywords: Magnetohydrodynamics, Quasi-static hypothesis, 2D turbulence, Direct Numerical Simulations

[a)] benjamin.favier@ec-lyon.fr; `http://lmfa.ec-lyon.fr/index.php?name=benjamin.favier`

I. INTRODUCTION

In most geophysical and astrophysical flows, turbulence is affected by forces that distort significantly some of its scales in an anisotropic manner, such as the Lorentz force arising from the presence of an external magnetic field in a conducting fluid. This specific turbulent dynamics forced by an imposed magnetic field is found in liquid metals flows, be they of geophysical nature—the melted iron core of the earth—or of academic interest in the laboratory[1]. More recent laboratory experiments use sodium or gallium, whereas liquid sodium is used in industrial configurations (such as a French fast breeder reactor Superphénix).

Generally, the motion of turbulent liquid metals is governed by magnetohydrodynamics (MHD): an induction equation for the fluctuating magnetic field ought to be coupled to the Navier-Stokes equations, and the latter equations are modified in turn by the Lorentz force, as a feedback from the magnetic field. In the presence of an external magnetic field, such MHD coupling results in new dissipative terms, of Ohmic nature, and selectively damped waves, the Alfvén waves[2]. In these cases (liquid metal), the magnetic diffusivity in the induction equation is greater than the molecular viscosity in the Navier-Stokes equations (*i.e.* the magnetic Prandtl number is small compared to one).

As discussed in section II, if, in addition, the magnetic Reynolds number is small enough, the linear regime no longer admits Alfvén waves solutions, and the effect of the Lorentz force reduces to anisotropic ohmic (or Joule) dissipation term. In this approximation, the induction equation is so drastically simplified that it does not require a specific study at all.

Forgetting the possible inhomogeneities arising from the presence of boundaries or interfaces in the latter flows, the fact is that homogeneous anisotropic turbulence remains far less studied than isotropic turbulence. In the context of low magnetic Reynolds numbers, the response of initially isotropic turbulence to a static magnetic field is nonetheless documented, in pioneering theoretical works[2], many numerical[3–6] and experimental studies[1]. One of the main properties of this kind of flow is the suppression of the three-dimensional motion due to anisotropic linear Joule dissipation, leading to a flow without variations in the direction of the imposed magnetic field. In the linear and inviscid regime, this final state is characterized by the following scaling of the vertical fluctuating velocity component w,

along the magnetic field, and the horizontal ones u and v:[2]

$$\left\langle w^2 \right\rangle \simeq \left\langle u^2 \right\rangle + \left\langle v^2 \right\rangle . \tag{1}$$

However, recent numerical simulations of low magnetic Reynolds number turbulence show that the horizontal kinetic energy is dominant, at least at large scales[5,7]. In the latter articles, the departure from equation (1) may be due to forcing schemes used to maintain the turbulence in a quasi-steady state. Another explanation proposed by Knaepen *et al.*[8] is that molecular viscosity might play a role in the decay of quasi-static MHD turbulence. Note that the decrease of the kinetic energy along the magnetic field has also been reported in a model based on the quasi-static approximation, but incorporating a non-isotropic model for viscous dissipation[9]. In this article, we present results of Direct Numerical Simulations (DNS) in order to analyze this nonlinear phenomenon, which is up to now considered as a restoration of isotropy, but still has to be elucidated[10].

II. GOVERNING EQUATIONS AND NUMERICAL SIMULATIONS

We consider initially isotropic homogeneous turbulence in an incompressible conducting fluid, in which $u \simeq v \simeq w$ The fluid is characterized by a kinematic viscosity ν, a density ρ and a magnetic diffusivity $\eta = (\sigma\mu_0)^{-1}$; σ is the electrical conductivity, μ_0 the magnetic permeability. The initial *rms* velocity is u_0, the integral length scale l_0. The Reynolds number and its magnetic counterpart are $Re = (u_0 l_0)/\nu \gg 1$ and $R_M = (u_0 l_0)/\eta \ll 1$. The flow is submitted to a uniform vertical magnetic field $\boldsymbol{B}_0$ scaled as Alfvén speed as $\boldsymbol{B}_0 = \boldsymbol{B}/\sqrt{\rho\mu_0}$. The ratio between the eddy turnover time and the Joule time is the magnetic interaction number $N = (B_0^2 l_0)/(\eta u_0)$. Within the quasi-static approximation, which implies that the asymptotic limit R_M goes to zero, but is nonetheless valid for $R_M < 1$,[8] the Navier-Stokes equations become

$$\frac{\partial \boldsymbol{u}}{\partial t} + \boldsymbol{u}\cdot\nabla\boldsymbol{u} = -\frac{1}{\rho}\nabla p + \nu\nabla^2\boldsymbol{u} + \underbrace{\frac{B_0^2}{\eta}\Delta^{-1}\frac{\partial^2 \boldsymbol{u}}{\partial z^2}}_{\boldsymbol{F}} \tag{2}$$

where $\boldsymbol{F}$ is the rotational part of the Lorentz force, Δ^{-1} is the inverse of the Laplacian operator and z the vertical coordinate, along the direction of $\boldsymbol{B}_0$. Compressible effects are not taken into account here, so that $\nabla\cdot\boldsymbol{u} = 0$. A pseudo-spectral method is used to solve

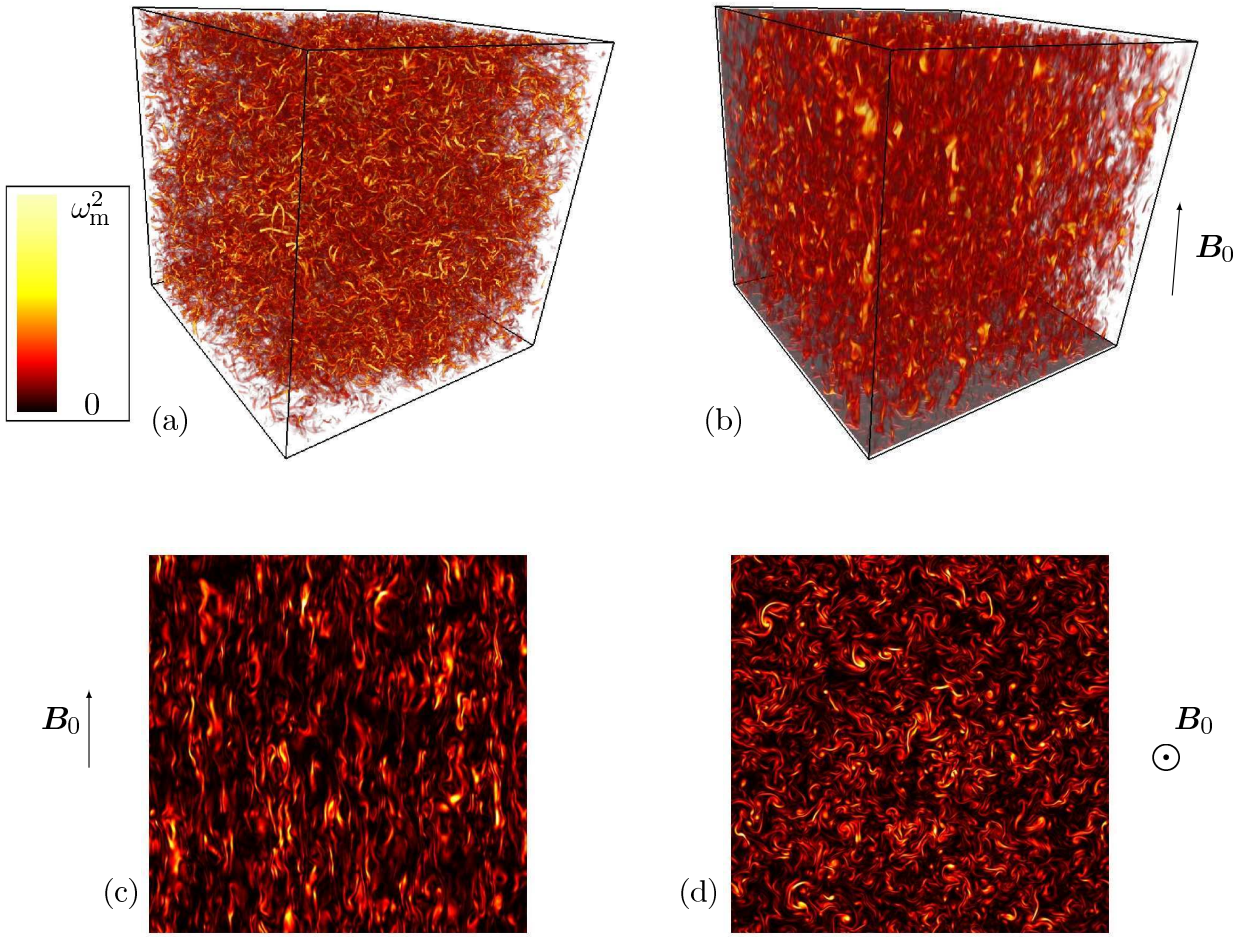

FIG. 1. Volume rendering of the enstrophy ($\omega_{\rm m}^2$ is about 25% of the maximum value) using VAPOR[11]. The resolution is 512^3 (see section IV). (a) Initial isotropic condition. (b) Final state for $N = 5$ (the vertical correlation length is roughly one tenth of the numerical box). (c) Vertical plane extracted from figure (b). (d) Horizontal plane extracted from figure (b).

equation (2). The velocity field is computed in a cubic box of side 2π with periodic boundary conditions using 256^3 Fourier modes. A spherical 2/3-truncation of Fourier modes is used to avoid aliasing and the time scheme is third-order Adams-Bashforth. The dissipative terms are solved implicitly. The Eulerian velocity field is initialized using an isotropic pre-computation of eq.(2) in the hydrodynamic case, *i.e.* $B_0 = 0$. The initial incompressible velocity field is a random superposition of Fourier modes distributed with a narrow-band kinetic energy spectrum $E(k, t = 0) \simeq k^4 \exp(-2(k/k_i)^2)$ peaked at k_i. Due to the imposed magnetic field, the vertical velocity correlation lengths quickly increase. We therefore avoid interferences with the periodic boundary conditions by choosing k_i larger than for a

hydrodynamic simulation. At the small-scale end of the spectrum, the minimum value of $k_{\max} l_\eta$ is 1.2 for all our computations[12], with l_η the Kolmogorov length scale. At the end of the pre-computation stage, the *rms* velocity is $u_0 = 0.45$ and the integral scale $l_0 = 0.16$ yielding $Re \simeq 100$. In the context of quasi-static MHD turbulence, it is not possible, at least using DNS, to perform high Reynolds number simulations without artificial effect of the periodic boundary conditions. We adopt here an intermediate configuration with moderate value of the Reynolds number and with no noticeable effect of the boundary conditions (see discussion on section III C). Note that spectral closures such as EDQNM may propose an interesting alternative, reaching high Reynolds numbers and forgetting about possible confinement effects from boundary conditions[13].

The corresponding turbulent flow field is used as initial state for three different MHD simulations. In all of them $R_M \simeq 0.1$ (hence $\eta \simeq 1$), so that the quasi-static approximation is justified[8]. Three different amplitudes of the imposed magnetic field are chosen, that correspond to three values of the interaction parameter: $N = 1$, 3 and 5. For each case, we perform additional "linear" simulations by neglecting the nonlinear advective term in eq.(2). The simulations are freely decaying, since forcing would hinder the natural development of anisotropy, which is the focus of this work.

III. RESULTS FOR THE QUASI-STATIC CASE

A. Kinetic energy and Reynolds stress tensor

Figure 2 presents the ratio between vertical and horizontal energy for different interaction parameters. The linear state characterized by eq. (1) is indeed observed when nonlinear interactions are removed. In the nonlinear simulations, the horizontal kinetic energy decays slower than the vertical one, which is consistent with previous observations[5,7].

In order to identify the origin of this phenomenon, we study the evolution of the Reynolds stress tensor $R_{ij} = \langle u_i(\boldsymbol{x}) u_j(\boldsymbol{x}) \rangle$ and its anisotropic contents $b_{ij} = R_{ij}/(2\mathcal{K}) - \delta_{ij}/3$ where $\mathcal{K}$ is the total kinetic energy and δ_{ij} is the Kronecker symbol. Considering the axisymmetry of the flow about the axis of $\boldsymbol{B}_0$, only one of the diagonal terms is relevant[14]. Figure 3(a) plots the time-dependent $b_{33}(t)$ for the three values of N. The index 3 stands for the vertical direction. The initial value $b_{33}(t = 0) = 0$ is characteristic of isotropic turbulence. In the

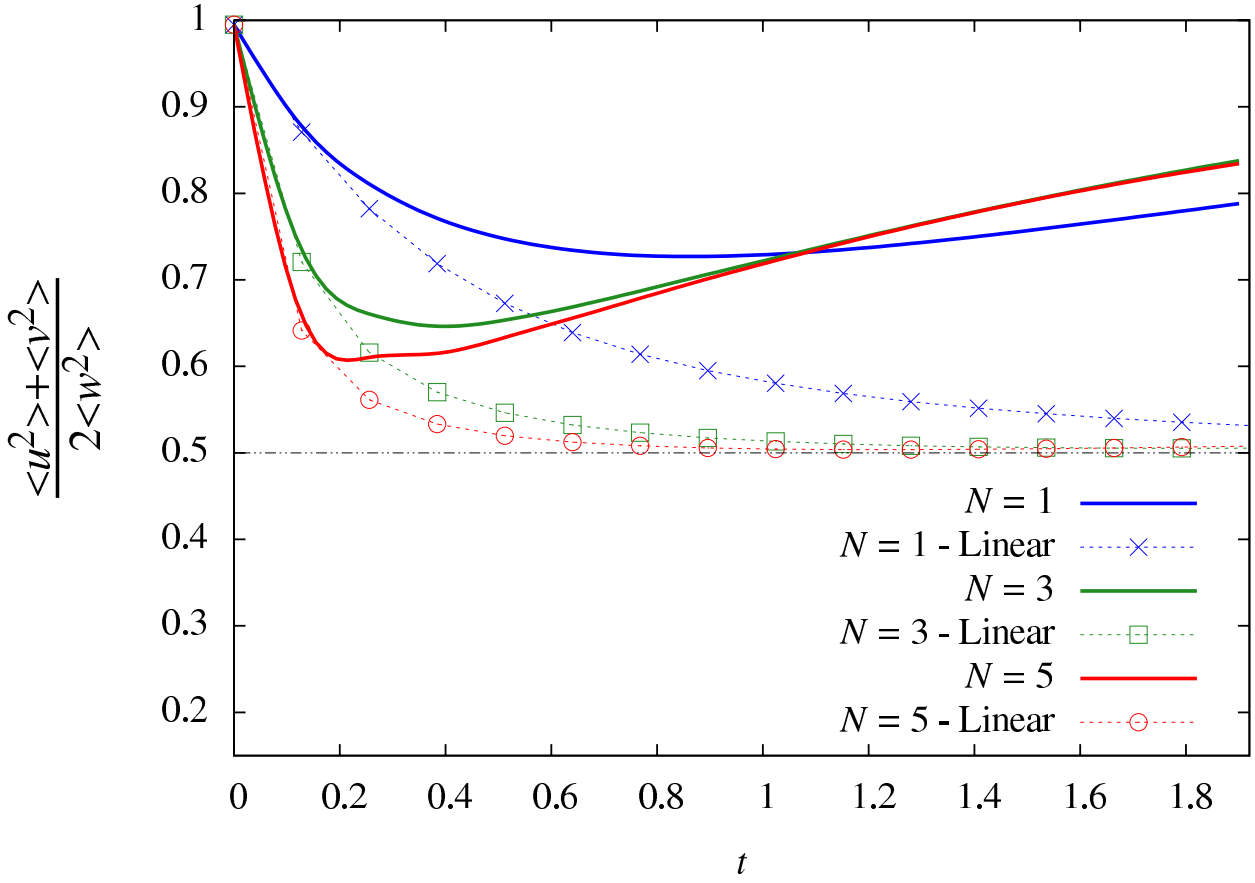

FIG. 2. Ratio between horizontal (perpendicular to the imposed magnetic field) and vertical (along $\boldsymbol{B}_0$) kinetic energy versus time. Continuous lines correspond to nonlinear simulations whereas dotted lines correspond to linear simulations (*i.e.* the non-linear advective term in eq.(2) is removed).

linear regime (symbols in figure 3(a)), b_{33} quickly recovers $b_{33} \simeq 1/6$ corresponding to the scaling in eq. (1). After a short initial growth—the larger N, the shorter this transient stage—, the nonlinear simulations exhibit a decay of b_{33}. This indicates that the vertical kinetic energy decays faster than the total kinetic energy, in agreement with figure 2. This observation alone could lead to the incorrect conclusion that the quadratic nonlinearity in eq.(2) tends to restore 3D isotropy. A closer inspection of b_{33} provides a significantly different viewpoint, when considering the decomposition of $b_{33} = b^e_{33} + b^{\mathcal{Z}}_{33}$ in directional and polarization anisotropy contributions[15,16], following:

$$b^e_{33} = \frac{1}{2\mathcal{K}} \int \left(e(\boldsymbol{k}) - \frac{E(k)}{4\pi k^2} \right) \sin^2\theta \mathrm{d}^3\boldsymbol{k} \tag{3}$$

$$b^{\mathcal{Z}}_{33} = \frac{1}{2\mathcal{K}} \int \mathcal{Z}(\boldsymbol{k}) \sin^2\theta \mathrm{d}^3\boldsymbol{k} \tag{4}$$

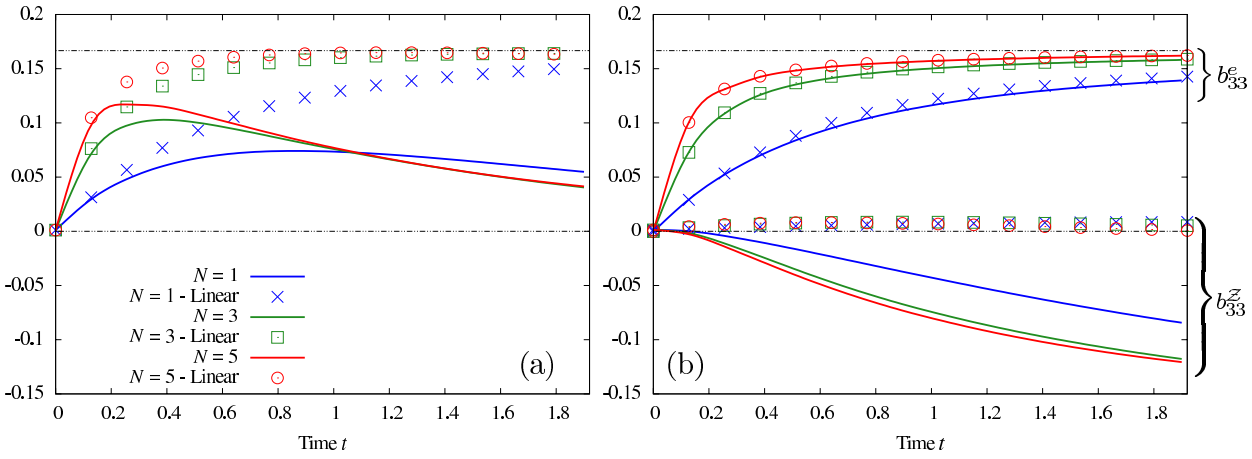

FIG. 3. Anisotropy tensor of the Reynolds stresses versus time. (a) $b_{33}(t)$. (b) $b^e_{33}(t)$ and $b^{\mathcal{Z}}_{33}(t)$.

where θ is the polar angle between the wave vector $\boldsymbol{k}$ and the axis of symmetry, $E(k)$ is the spherically-averaged kinetic energy spectrum, $\mathcal{Z}(k)$ is the polarization spectrum (see below). This decomposition is easier described in polar-spherical coordinates (see figure 4) with unit toroidal vector $\boldsymbol{e}^{(1)}$ and poloidal vector $\boldsymbol{e}^{(2)}$. Due to incompressibility $\hat{\boldsymbol{u}}(\boldsymbol{k})\cdot\boldsymbol{k}=0$, $\hat{\boldsymbol{u}} = \hat{u}^{(1)}\boldsymbol{e}^{(1)} + \hat{u}^{(2)}\boldsymbol{e}^{(2)}$: each Fourier mode has a toroidal contribution $\hat{u}^{(1)}$ and a poloidal one $\hat{u}^{(2)}$ (we drop the explicit $\boldsymbol{k}$ dependence in this paragraph). Assuming horizontal plane mirror symmetry, thus without helicity, the kinetic energy density is

$$e = E^{\mathrm{pol}} + E^{\mathrm{tor}} = \frac{1}{2}\left(\hat{u}^{(2)*}\hat{u}^{(2)} + \hat{u}^{(1)*}\hat{u}^{(1)}\right) \tag{5}$$

and the polarization tensor density is

$$\mathcal{Z} = E^{\mathrm{pol}} - E^{\mathrm{tor}} \ . \tag{6}$$

A detailed presentation of this decomposition can be found in[15]. Note that b^e_{33} is close to the so-called Shebalin angle[17], whereas b^e_{ij} is shown[16] to be exactly minus half the non-dimensional deviator of the "dimensionality tensor"[9].

Figure 3(b) shows the time evolution of b^e_{33} and $b^{\mathcal{Z}}_{33}$. For all values of N, b^e_{33} increases indicating that the kinetic energy density $e(\boldsymbol{k})$ is not isotropically distributed among the different wavevector orientations. In the linear runs (symbols in figure 3) b^e_{33} follows closely the nonlinear evolution (continuous lines in figure 3). Unlike b^e_{33}, a departure is observed for $b^{\mathcal{Z}}_{33}$: it decreases in the nonlinear simulations, but remains negligible in the linear runs. Thus, the decay of b_{33} observed in figure 3(a) is due to a nonlinear decay of the polarization contribution $b^{\mathcal{Z}}_{33}$.

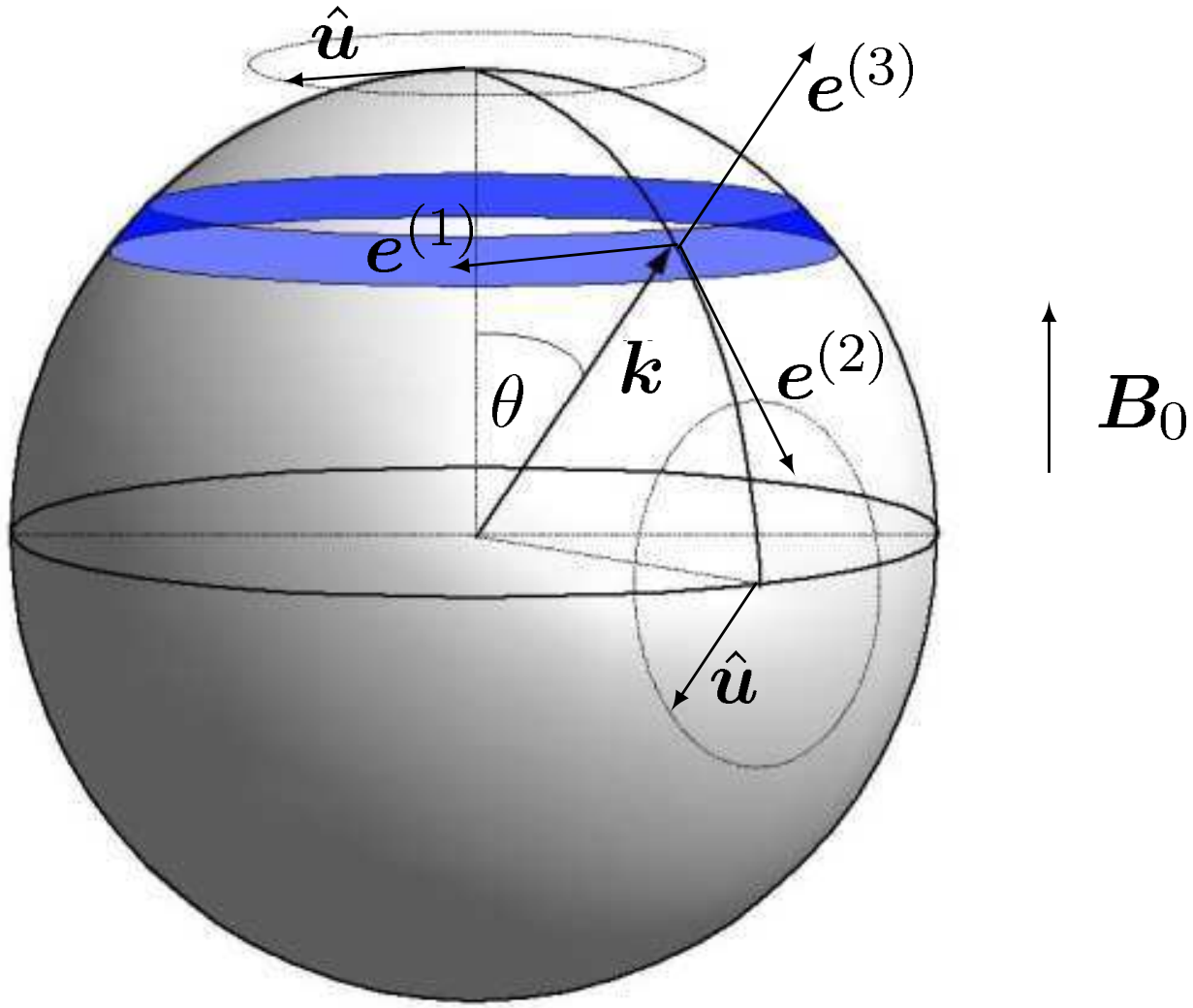

FIG. 4. Craya-Herring frame $(\boldsymbol{e}^{(1)}, \boldsymbol{e}^{(2)}, \boldsymbol{e}^{(3)})$ in Fourier space. Fourier modes in the blue region contribute to $E(k,\theta)$ (eq.(7)). The polar modes (*i.e.* $\theta \simeq 0$) contribute to horizontal kinetic energy, whereas equatorial modes (*i.e.* $\theta \simeq \pi/2$) contribute to both vertical (along $\boldsymbol{e}^{(2)}$) and horizontal (along $\boldsymbol{e}^{(1)}$) kinetic energies.

The analysis can be even more refined when considering the scale dependence of the poloidal/toroidal anisotropy. In eq.(2), one observes that the Lorentz force introduces an additional anisotropic dissipation, upon examining the Fourier transform of $\boldsymbol{F}$: $\hat{\boldsymbol{F}} = -\left(\boldsymbol{B}_0 \cdot \boldsymbol{k}\right)^2 \hat{\boldsymbol{u}} / \left(\eta k^2\right)$ shows that the vertical modes ($\boldsymbol{k} // \boldsymbol{B}_0$) are strongly damped whereas horizontal ones ($\boldsymbol{k} \perp \boldsymbol{B}_0$) are only modified by pressure effects. This well-known phenomenon, which is linear and characterized by a Joule timescale $\tau_J = \eta / B_0^2$, is responsible for the initial growth of b^e_{33} observed in figure 3(a). Note that τ_J can be used to rescale t (as

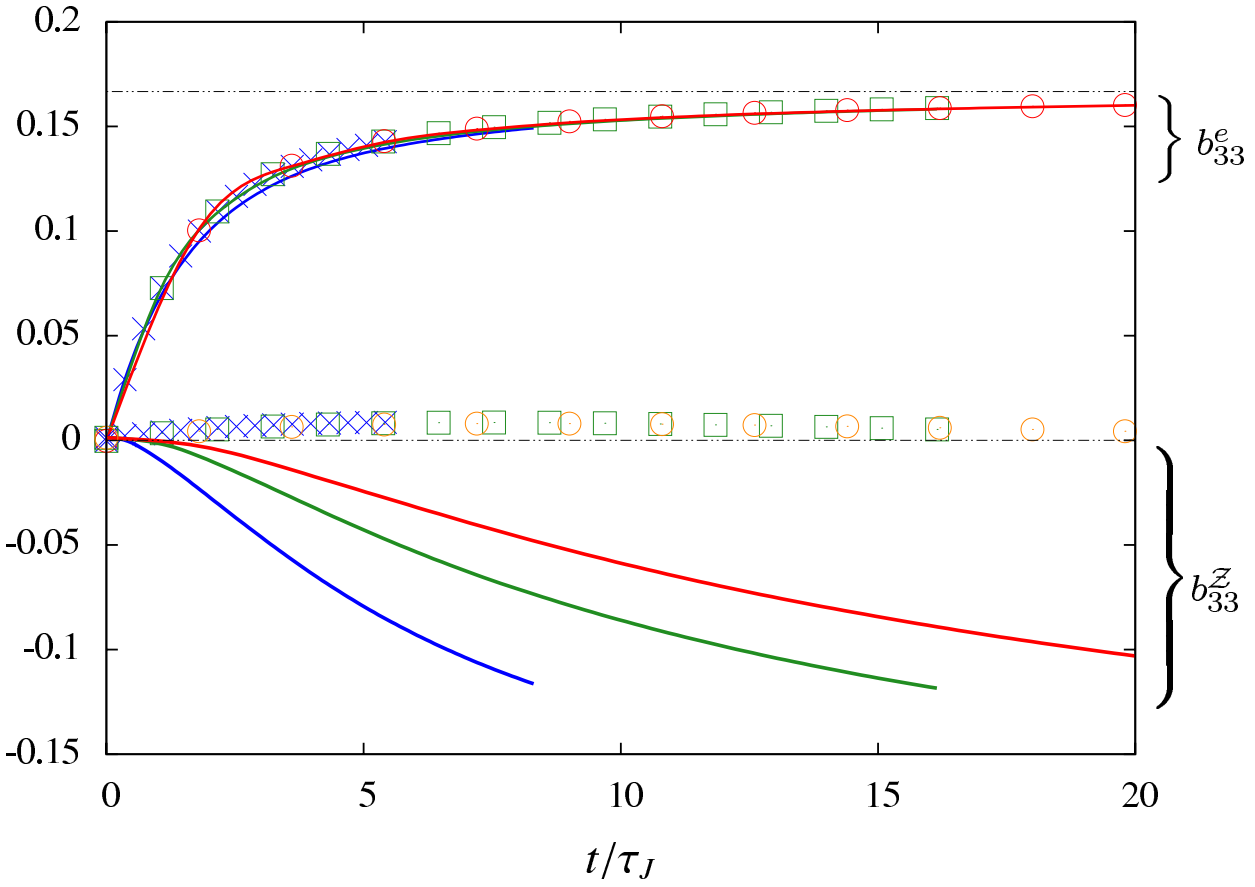

FIG. 5. Same as figure 3(b) but with time normalized by the Joule timescale $\tau_J = \eta/B_0^2$.

in figure 5) so that all curves for b^e_{33} collapse. However, with this scaling, the evolution of b^Z_{33} is still very different for the various cases. As N increases (*i.e.* the nonlinear interactions become more and more negligible compared to linear ohmic dissipation), the decay of b^Z_{33} is slower, clearly indicating that the polarization effect is triggered by a nonlinear phenomenon.

B. Angular energy spectra

Let us define angular energy spectra defined by

$$E(k,\theta) = f(\theta) \sum_{T(k,\theta)} \hat{\boldsymbol{u}} \cdot \hat{\boldsymbol{u}}^* \ , \tag{7}$$

where $T(k,\theta)$ denotes the torus-shaped volume defined from $k - \Delta k/2 < |\boldsymbol{k}| < k + \Delta k/2$ and $\theta - \Delta\theta/2 < \theta < \theta + \Delta\theta/2$, with $\Delta k = 1$ and $\Delta\theta = \pi/10$ the Fourier space discretization steps (blue domain in figure 4). $f(\theta)$ is the geometrical weighting function such that the angular spectra collapse in isotropic turbulence. Torus-averaged angular spectra $E(k,\theta)$

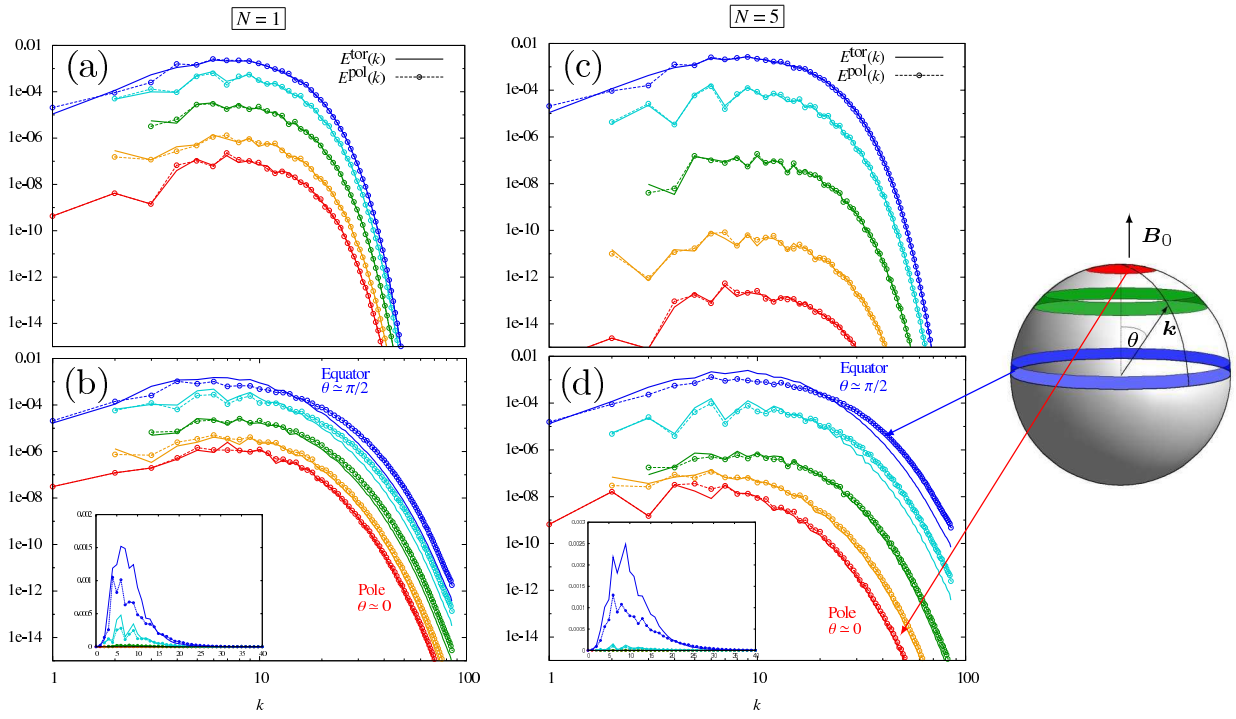

FIG. 6. Angular energy spectra (note that for the case $N = 5$, the results are plotted for $t \simeq 20\tau_J$ whereas for the case $N = 1$, it corresponds to $t \simeq 5\tau_J$). Top: Linear simulations. Bottom: Nonlinear simulations. Left (figures (a) and (b)): $N = 1$. Right (figures (c) and (d)) $N = 5$. On figures (b) and (d), the embedded figures corresponds to the same results presented in linear scale.

have already been used in the context of rotating turbulence[16] and are similar to the so-called ring decomposition[6]. On figures 6, we present the angular spectra for five orientations from the equator ($\theta \simeq \pi/2$) to the pole ($\theta \simeq 0$), for $N = 1$ (figures 6(a) and (b)) and $N = 5$ (figures 6(c) and (d)). In addition, we distinguish the poloidal and toroidal spectra $E^{\rm pol}$ and $E^{\rm tor}$, and the linear simulations from the nonlinear ones (figures 6(a)(c) and figures 6(b)(d) respectively). The figures show that almost all the energy is concentrated in the equatorial spectrum, as a result from the linear Joule dissipation, independently on the poloidal or toroidal contributions, and in both the linear and nonlinear simulations. The reasons for the observed differences between the latter two cases are two-fold: *(a)* the nonlinear downscale energy cascade increases the energy in the small scale range of the nonlinear runs with respect to the linear ones; *(b)* in the meantime, a nonlinear angular transfer kicks in, explaining the polar energy depletion, in the same figures, for the linear runs (see *e.g.*[6]). Given that polar modes contribute only to the horizontal kinetic energy (clearly from geometrical reasons,

see fig.4) combined with a more efficient Joule dissipation in the same region, this linear mechanism is responsible for the rapid decrease of horizontal energy, *i.e.* rapid *increase* of b_{33}, observed at short times on fig.3(a). There is however nothing in this mechanism that explains the decay, of $b_{33}^{\mathcal{Z}}$ in the nonlinear simulation results plotted on fig.3(b).

The crucial difference between linear and nonlinear simulations in figures 6 is brought to light by the poloidal-toroidal decomposition. At the equator in the full DNS, the horizontal kinetic energy (also $E^{\rm tor}$ at this specific orientation) is dominant at large scales, whereas the vertical kinetic energy (also $E^{\rm pol}$) is dominant at small scales (the small plot in inset of figures 6(b) and (d), in linear scale, shows more clearly the important large-scale energy gap between the two modes). This result explains the increase of horizontal kinetic energy with respect to the vertical energy, hence the decay of $b_{33}^{\mathcal{Z}}$. It is clearly of nonlinear origin since it disappears when nonlinear interactions are removed (see figures 6(a) and (c)). Although already observed in previous works[7], this unpredicted dominance of horizontal energy was not understood. We provide here a more precise analysis since only modes such that $\boldsymbol{k} \perp \boldsymbol{B}_0$ appear to have noticeably different poloidal and toroidal energies.

C. Correlation lengths

We present in this paragraph some results about correlation lengths, which can be computed directly from the angular dependent spectra, and we thus check that our simulations are free from any artificial confinement due to periodic boundary conditions. Let us introduce the velocity correlation lengths defined by

$$L_{ij}^{l} = \frac{1}{\langle u_i u_j \rangle} \int_0^\infty \langle u_i(\boldsymbol{x}) u_j(\boldsymbol{x}+\boldsymbol{r}) \rangle \, \mathrm{d}r \tag{8}$$

where $r_k = r\delta_{kl}$ is the two-point separation. In the current axisymmetric configuration, the most relevant anisotropy indicators involve the integral length scale with vertical separation but relative to either vertical or horizontal velocity components[15]:

$$L_{33}^{3} = \frac{2\pi^2}{u_3^2} \int_0^\infty \left[e(\boldsymbol{k}) + \Re\mathcal{Z}(\boldsymbol{k}) \right] \Big|_{k_z=0} k \mathrm{d}k \tag{9}$$

$$L_{11}^{3} = \frac{\pi^2}{u_1^2} \int_0^\infty \left[e(\boldsymbol{k}) - \Re\mathcal{Z}(\boldsymbol{k}) \right] \Big|_{k_z=0} k \mathrm{d}k \ . \tag{10}$$

The correlation length L_{11}^3 is characterized by the most critical growth rate, as qualitatively observed on visualizations 1(b) and (d). At the end of the simulations (*i.e.* for $t \approx 1.8$),

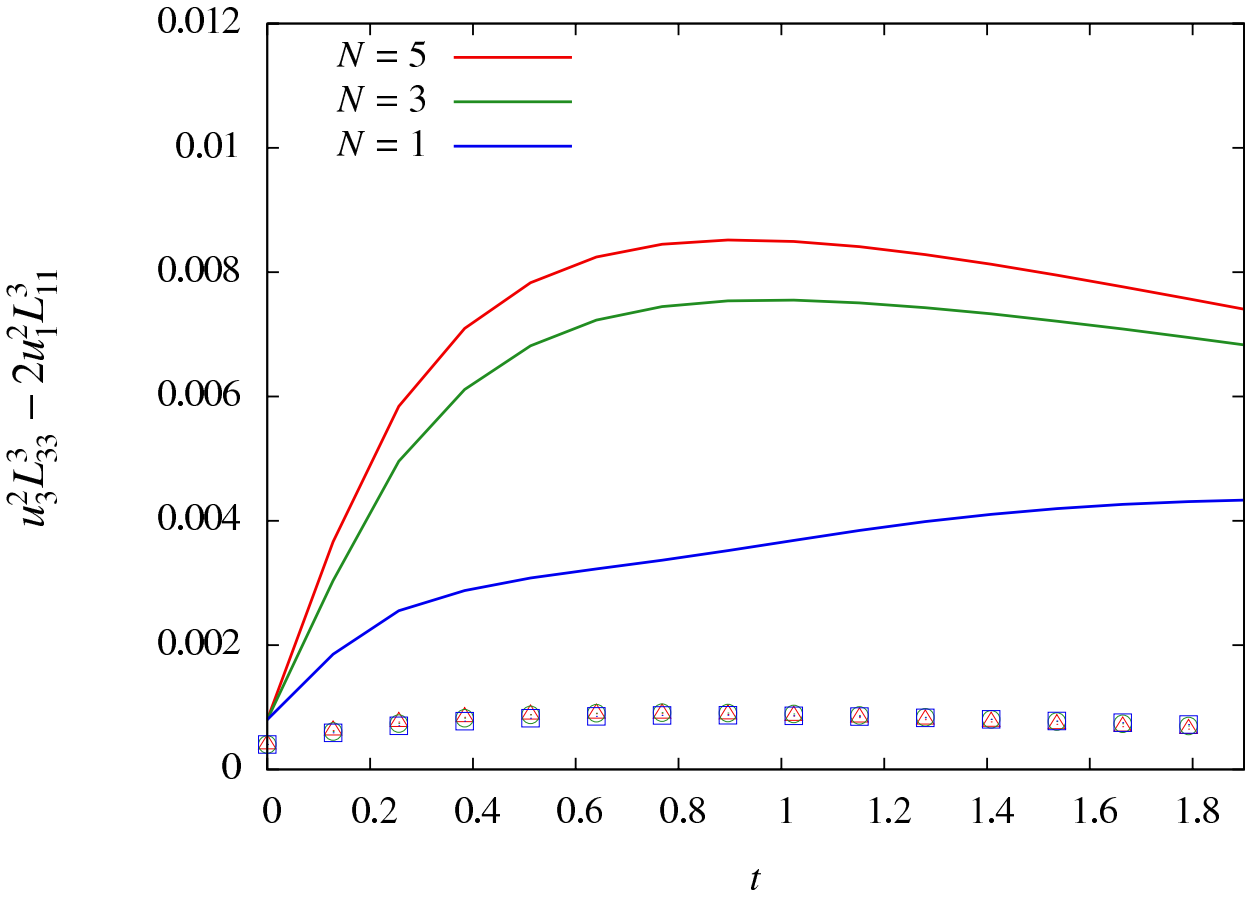

FIG. 7. Evolution with time of the quantity $u_3^2 L_{33}^3 - 2u_1^2 L_{11}^3$. The nonlinear results are represented in continuous lines and linear results in symbols.

$L_{11}^3 \approx 2,\ 1.6,\ 1$ for the respective cases $N = 5,\ 3,\ 1$. In all cases, L_{11}^3 is significantly smaller than the box size 2π, except for $N = 5$ for which the largest integral scale is about one third of the numerical box size. However, we have seen that the results for the case $N = 1$ and $N = 5$ are qualitatively very similar (see for example figures 6). We are therefore confident in the fact that our simulations are free from any spurious periodic effects.

Moreover, it is possible to isolate the contribution due to polarization looking at the quantity:

$$u_3^2 L_{33}^3 - 2u_1^2 L_{11}^3 = \int_0^\infty 4\pi^2 \Re \mathcal{Z}(\boldsymbol{k})\Big|_{k_z=0} k \mathrm{d}k \ , \tag{11}$$

plotted on figure 7. This quantity has two main advantages: computing from equations (9) and (10), its departure from zero is only due to the polarization $\mathcal{Z}(\boldsymbol{k})$; secondly, this quantity is accessible experimentally and is thus of particular interest. Again, one observes on figure 7 that polarization is negligible in the linear case whereas a significant growth is

observed in the nonlinear case.

In short, the anisotropic Lorentz force is responsible for a preferential dissipation leading to a turbulent flow independent of the vertical direction (see figure 1(b)); this linear effect concentrates the kinetic energy among horizontal modes, as attested by the growth of b_{33}^e. Then, due to nonlinearity, the energy is anisotropically distributed among poloidal and toroidal components leading to a nonzero polarization and negative b_{33}^z.

IV. THE ANALOGY WITH 2D-3C TURBULENCE

The quasi-static MHD turbulence is however far from being purely two-dimensional. Although the flow tends to be invariant in the vertical direction, the vertical kinetic energy is not negligible compared to the horizontal one (and is even dominant in the linear regime). This state is often referred to as two-dimensional, three-components (2D-3C) or "two-and-a-half-dimensional" turbulence[18]. We now propose a simple description of the above results on directional anisotropy and polarization. We first write the Navier-Stokes equations for a flow independent of the vertical direction z, so that $\partial/\partial z = 0$:

$$\frac{\partial w}{\partial t} + \boldsymbol{u}_\perp \cdot \nabla_\perp w = \nu \nabla_\perp^2 w \tag{12}$$

$$\frac{\partial \boldsymbol{u}_\perp}{\partial t} + \boldsymbol{u}_\perp \cdot \nabla_\perp \boldsymbol{u}_\perp = -\frac{1}{\rho}\nabla_\perp p + \nu \nabla_\perp^2 \boldsymbol{u}_\perp \tag{13}$$

where $\boldsymbol{u}_\perp = (u, v)$ is the horizontal velocity component and $\nabla_\perp$ the horizontal gradient. In both equations, the Lorentz force disappears altogether. Eq.(12) for the vertical velocity is that of a passive scalar, whereas eq.(13) for horizontal velocity is characteristic of 2D hydrodynamic turbulence. One therefore expects an inverse energy cascade for the horizontal velocity (or at least a strongly attenuated direct cascade) and a classical direct cascade for the vertical velocity. This is consistent with the results observed on figures 6(b) and (d) since the slope of the toroidal (*i.e.* horizontal) component is steeper than the slope of the poloidal (*i.e.* vertical) component for horizontal modes (*i.e.* at the equator). Thus, we explain the large-scale dominance of horizontal energy as a result of 2D-like cascade for the horizontal velocity. The vertical component behaves like a passive scalar, and is therefore characterized by a direct cascade so that the vertical energy is dominant at small scales. Note that this effect has nothing to do with a restoration of isotropy, even if b_{33} tends to its isotropic value.

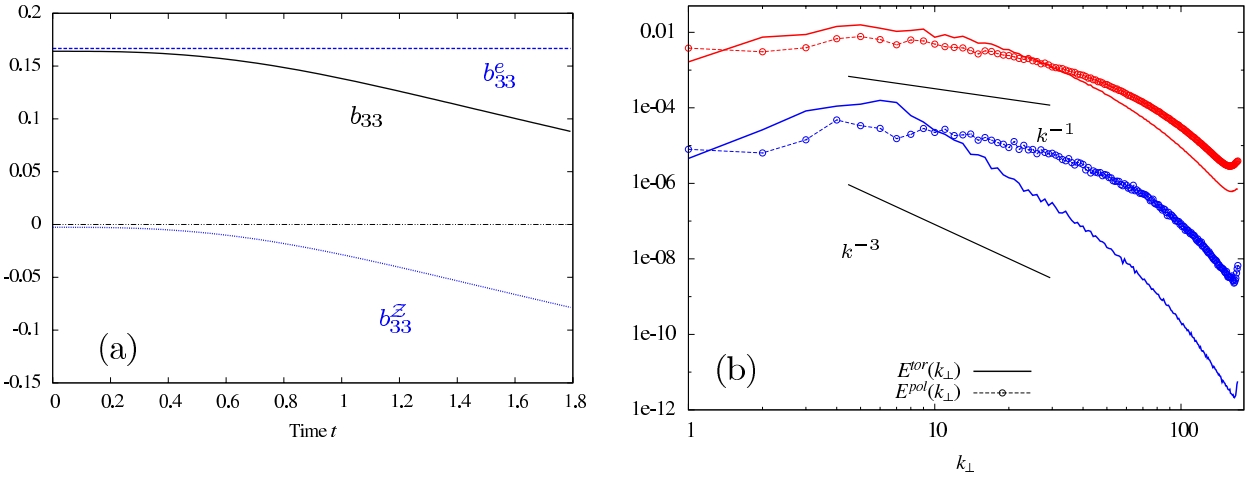

FIG. 8. (a) $b_{33}(t)$ from a 2D-3C simulation. (b) Equatorial energy spectra $E^{\rm pol,tor}(k_\perp)$. Red/top: Quasi-static 3D MHD using 512^3 Fourier modes. Blue/bottom: 2D-3C simulation using 512^2 Fourier modes (shifted down by two decades).

To assess the validity of this analysis, we perform two additional simulations. First, we compute the evolution of hydrodynamic turbulence from an initial 2D-3C state and a resolution of 512^2. Figure 8(a) shows that $b^e_{33} = 1/6$ during all the simulation. As in quasi-static MHD turbulence, 2D-3C turbulence is characterized by a negative polarization indicating a dominance of toroidal kinetic energy with respect to the poloidal one. Figure 8(b) shows the equatorial toroidal and poloidal energy spectra $E^{\rm tor,pol}(k_\perp)$ (bottom of the figure) that again exhibit a dominance of toroidal energy at large scales and the opposite at small scales, in support to our previous analysis on the final state of quasi-static MHD turbulence. Secondly, we would like to validate the universality of the mechanism at higher Reynolds number MHD turbulence, by performing a quasi-static simulation at $Re \simeq 300$, using 512^3 Fourier modes. We choose the case $N = 5$ and $R_M = 0.1$. In this 3D simulation, the crossing of the toroidal and poloidal spectra (top spectra in figure 8(b)) appears as in figures 6(b) and (d) and in the previously described 2D-3C spectra. The k^{-3} and k^{-1} slopes are plotted for comparison with common scalings of 2D turbulence with passive scalar[19,20], again showing clearly that the energy cascade is more efficient for the toroidal energy than for the poloidal one, resulting in a steeper slope for toroidal kinetic energy. Of course, many differences arise looking at figure 8(b). This is due to the fact that quasi-static turbulence is not purely invariant in the vertical direction (see visualization on fig.1(b)).

V. CONCLUSION

In conclusion, we have found indications that the final state of quasi-static MHD turbulence, reached after a time sufficient for developping a strong anisotropy, is analogous to 2D-3C hydrodynamic turbulence. The mechanism responsible for the transition from 3D isotropic turbulence to 2D-3C turbulence is subtle. It combines the anisotropic Joule dissipation, which is a linear phenomenon, and nonlinear energy transfers. If nonlinearities are neglected, this final state is characterized by a dominance of vertical kinetic energy[2]. However, from the quasi-2D state arising from Joule dissipation, nonlinearity induces different dynamics for toroidal/horizontal velocity components and for poloidal/vertical components. The horizontal flow behaves like 2D turbulence whereas the vertical flow behaves like a passive scalar advected by 2D turbulence. Accordingly, the energy cascade (and thus the dissipation) is more efficient in the vertical direction, explaining the overall dominance of horizontal energy. We have also shown that the poloidal/toroidal decomposition and the distinction between directional and polarization anisotropy are fundamental to explain these physical phenomena. This description may help to explain the large scale anisotropy of some geophysical or astrophysical conducting fluid flows, with the possibility of coupling the 2D-3C model for the large scales to a specific turbulence closure at small scales, thus allowing to achieve very high Reynolds number simulations.

The authors thank the computing center IDRIS of CNRS for the allocation of cpu time under project numbers 071433 and 022206.

REFERENCES

[1]A. Alemany, R. Moreau, P.L. Sulem and U. Frisch. *Influence of an external magnetic field on homogeneous MHD turbulence* J. de Mécanique **18**, 277–313 (1979).

[2]H.K. Moffatt. *On the suppression of turbulence by a uniform magnetic field* J. Fluid Mech. **28**, 571–592 (1967).

[3]U. Schumann. *Numerical simulation of the transition from three- to two-dimensional turbulence under a uniform magnetic field* J. Fluid Mech. **74**, 31–58 (1976).

[4]O. Zikanov and A. Thess. *Direct numerical simulation of forced MHD turbulence at low magnetic Reynolds number* J. Fluid Mech. **358**, 299–333 (1998).

[5]A. Vorobev, O. Zikanov, P.A. Davidson and B. Knaepen. *Anisotropy of MHD turbulence at low magnetic Reynolds number* Phys. Fluids **17**, 125105 (2005).

[6]P. Burattini, M. Kinet, D. Carati and B. Knaepen. *Spectral energetics of quasi-static MHD turbulence* Physica D **237**, 2062–2066 (2008).

[7]P. Burattini, M. Kinet, D. Carati and B. Knaepen. *Anisotropy of velocity spectra in quasistatic magnetohydrodynamic turbulence* Phys. Fluids **20** (065110) (2008).

[8]B. Knaepen, S. Kassinos and D. Carati. *Magnetohydrodynamics turbulence at moderate Reynolds number* J. Fluid Mech. **513**, 199–220 (2004).

[9]S.C. Kassinos and W.C. Reynolds. *Structure-based modeling for homogeneous MHD turbulence* Center for Turbulence Research, Annual Research Briefs pages 301–315 (1999). Stanford/ NASA-Ames.

[10]B. Knaepen and R. Moreau. *Magnetohydrodynamics turbulence at low magnetic Reynolds number* Annu. Rev. Fluid Mech. **40**, 25–45 (2008).

[11]J. Clyne, P. Mininni, A. Norton and M. Rast. *Interactive desktop analysis of high resolution simulations: application to turbulent plume dynamics and current sheet formation* New J. of Physics **9**, 301 (2007).

[12]J. Jimenez, A.A. Wray, P.G. Saffman and R.S. Rogallo. *The structure of intense vorticity in isotropic turbulence* J. Fluid Mech. **255**, 65–90 (1993).

[13]C. Cambon and FS Godeferd. *Inertial transfers in freely decaying, rotating, stably stratified and MHD turbulence* AIAA Progress in Astronautics and Aeronautics Series (ed. H. Branover & Y. Unger) **162**, 150–168 (1993).

[14]In axisymmetric cases, only the b_{33} component is useful since all the others components are linked by the following relation[16]: $b_{ij}^{e,\mathcal{Z}} = -3(\delta_{ij}/3 - \delta_{i3}\delta_{j3})b_{33}^{e,\mathcal{Z}}/2$.

[15]C. Cambon and L. Jacquin. *Spectral approach to non-isotropic turbulence subjected to rotation* J. Fluid Mech. **202**, 295–317 (1989).

[16]C. Cambon, N. N. Mansour and F. S. Godeferd. *Energy transfer in rotating turbulence* J. Fluid Mech. **337**, 303–332 (1997).

[17]J.V. Shebalin, W.H. Matthaeus and D. Montgomery. *Anisotropy in MHD turbulence due to a mean magnetic field* J. Plasma Phys. **29**, 525 (1983).

[18]D. Montgomery and L. Turner. *Two-and-a-half-dimensional magnetohydrodynamic turbulence* Phys. Fluids **25(2)**, 345–349 (1982).

[19]G.K. Batchelor. *Small-scale variation of convected quantities like temperature in turbulent*

fluid J. Fluid Mech. **5**, 113 (1959).

[20]W.J.T. Bos, B. Kadoch, K. Schneider and J.-P. Bertoglio. *Inertial range scaling of the scalar flux spectrum in two-dimensional turbulence* Physics of Fluids **21** (11), 115105 (2009).